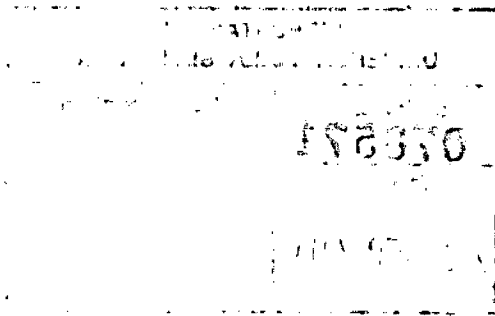


修士論文



# Prediction of maximum strain and strain rate in SHPB specimens based on energy analysis



岡山理科大学大学院

工学研究科

機械システム工学専攻 計測・制御工学研究室

T11TM07 ヌルイザトウル アティカ ビンティ ラマト

# **Prediction of maximum strain and strain rate in SHPB specimens based on energy analysis**

Nurizzatul Atikha binti Rahmat

## **(ABSTRACT)**

The split Hopkinson pressure bar (SHPB) technique developed by H. Kolsky has been widely used to determine stress-strain curves of materials at strain rates from  $10^2$  to  $10^4$  s<sup>-1</sup>. In the SHPB method, it is usually impossible to predict the maximum strain and strain rate obtainable in the specimen before testing even if an impact velocity of a striker bar, diameters and acoustic impedances ( $\rho c$ ) of the Hopkinson bars and the specimen geometry are specified. This is because the strain rate dependence of test materials is unknown until the SHPB tests are conducted. The objective of the present work is to predict the maximum plastic strain and strain rate in the SHPB specimen based on the energy analysis using rate-independent plasticity. Two different material models are used to express the rate-independent mechanical behavior of the test materials. The present energy analysis enables one to approximately estimate the maximum plastic strain and strain rate in the SHPB specimen in advance from the static properties of the test materials. The prediction accuracy of the energy analysis is checked by comparison with the experimental results for three high-strength aluminum alloys obtained from the SHPB tests. It is demonstrated that the maximum strain and strain rate in the SHPB specimens are slightly overestimated by the energy analysis due to the neglect of the kinetic energy within them.

# Contents

<b>1. Introduction</b>	<b>1</b>
<b>2. Experimental Details</b>	<b>2</b>
2.1. Test Materials.....	2
2.2. Design of Compression Specimens.....	4
2.3. Low Strain-Rate Compression Testing.....	5
2.4. High Strain-Rate Compression Testing.....	5
<b>3. Results and Discussion</b>	<b>10</b>
3.1. SHPB Test Results.....	10
3.2. Observation of Macrostructure and Microstructure of Test Materials.....	12
<b>4. Conclusions</b>	<b>13</b>
<b>Appendix</b>	<b>14</b>
A.1 Energy Analysis in the SHPB.....	14
A.2 Strain Rate Independent Models.....	16
A.2.1 Rigid Perfectly-Plastic Material Model.....	16
A.2.2 Rigid Plastic-Strain Hardening Material model.....	17
<b>References</b>	<b>19</b>

<b>Fig.3-10</b>	TEM pictures of microstructure in specimens: (a) AA2024-T3; (b) AA6061-T6; (c) AA7075-T651.....	30
<b>Fig.A-1</b>	Schematic illustration of wave propagation within striker bar and input bar.....	31
<b>Fig.A-2</b>	Stress-plastic strain relation for rigid perfectly-plastic material model.....	32
<b>Fig.A-3</b>	Stress-plastic strain relation for rigid plastic strain hardening material model.....	32

## List of Table captions

<b>Table 2-1</b>	Nominal tensile properties of three aluminum alloys tested.....	33
<b>Table 2-2</b>	Geometries of static and impact compression specimens of three different aluminum alloys.....	33
<b>Table 2-3</b>	Mechanical properties of striker bar and input/output bars.....	34
<b>Table 2-4</b>	Dimensions of striker bar and input/output bars.....	34
<b>Table 3-1</b>	Experimental and predicted results for strain rate and maximum plastic strain in SHPB specimens.....	35

# 1 Introduction

The split Hopkinson pressure bar (SHPB) originally developed by Kolsky in 1949 [1] has commonly been used to characterize the dynamic behavior of materials. The SHPB concept [2] can be adapted for compression, tension, torsion and bending tests at high strain rates. The available strain rate range of the technique depends on the mode of loading and on the dimensions of the specimen geometry. A strain-rate range of  $500 \text{ s}^{-1}$  to  $5000 \text{ s}^{-1}$  is mostly common in the SHPB tests. An excellent literature survey of various applications of the SHPB to composite materials is given in Ref. [3] In the conventional SHPB method, it is usually impossible to predict the maximum strain and strain rate obtainable in the SHPB specimen before testing even if an impact velocity of a striker-bar, diameters and acoustic impedances of the Hopkinson bars and the specimen geometry are given. This is because the strain rate dependence of test materials is unknown until the SHPB tests are performed. Accordingly, we have to adjust the impact velocity of the striker bar, the dimensions of the specimen for fixed dimensions and mechanical properties of the Hopkinson bars through performing several preliminary SHPB tests in attempts to examine the maximum plastic strain and strain rate in the SHPB specimen.

The purpose of the present work is to predict the maximum plastic strain and strain rate in the SHPB specimen from the energy analysis [4] using rate-independent plasticity. Three different aluminum alloys (AA2024-T3, AA6061-T6, and AA7075-T651) are chosen as rate-independent test materials for which two different material models are used to express their mechanical

behavior. The present analysis enables one to approximately estimate the maximum plastic strain and strain rate in the SHPB specimen in advance from the static properties of the test materials. The prediction accuracy of the analysis is checked by comparison with the experimental results for the three aluminum alloys obtained from the SHPB tests. It is demonstrated that the maximum strain and average strain rate in the SHPB specimens are slightly overestimated by the analysis due to the neglect of the kinetic energy within them.

## **2 Experimental Details**

### **2.1 Test Materials**

Structural impact has become increasingly relevant for various engineering fields such as aeronautical, naval and automotive industries. Among the materials traditionally investigated for building protection structures responsible for energy absorption in high loading rate events, the light weight alloys have particular interest. A considerably amount of scientific works has been published over the last decades dealing with the mechanical response of aluminum alloys subjected to impact loading. Those investigations answer to the requirements of the previously mentioned industrial sectors of replacing traditional steel alloys by such metallic materials with improved specific strengths. In particular, aluminum alloys have been widely used for automobile and aircraft structural components. This trend is enhanced by the key factor which represents fuel economy in design stages. These alloys have widely been applied in the aeronautical industry for construction of mechanical elements with elevated structural responsibility. The thermo mechanical behavior of the material is characterized in tension over a wide range of strain rate and temperature.

Aluminum alloys can be categorized into a number of groups based on the particular material's characteristics such as its ability to respond to thermal and mechanical treatment and the primary alloying element added to the aluminum alloy. In this present study, three different aluminum alloys (AA2024- T3, AA6061- T6, and AA7075- T651) were chosen as test materials. The nominal tensile properties of the three aluminum alloys are listed in **Table 2-1**.

AA2024-T3 is a heat treatable aluminum alloy, with Cu and Mg as the main alloying elements. The "T3" designation indicates that the alloy was solution-annealed, quenched, and aged at ambient temperatures to a substantially stable condition. It shows good machinability and surface finish capabilities. It is one of high-strength aluminum alloys with adequate workability and widely used in aircraft structures where stiffness, fatigue performance and good strength are required. Other applications comprise hydraulic valve bodies, missile parts, munitions, nuts or pistons.

AA6061-T6 is a precipitation hardening aluminum alloy, heat treatable, containing Mg and Si as its major alloying elements. The "T6" designation indicates that the alloy was solution heat treated and artificially aged. It has commonly been used in construction of aircraft structures, such as wings and fuselages, more commonly in homebuilt aircraft than commercial or military aircraft.

AA7075-T651 is also a heat treatable aluminum alloy, with Zn as the primary alloying element. The "T651" designation indicates that the alloy was solution heat treated, stress- relieved stretched, then

artificially aged (precipitation heat treatment). It is strong, with strength comparable to many steels, and has good fatigue strength and average machinability, but has less resistance to corrosion than many other Al alloys. Its relatively high cost limits its use to applications where cheaper alloys are not suitable. Due to its strength, high density, thermal properties and its ability to be highly polished, 7000 series alloys such as AA7075-T651 are widely used for highly stressed structural parts like aircraft fittings, gears and shafts, fuse parts, meter shafts and gears, missile parts, regulating valve parts, worm gears, keys, aircraft and aerospace. Their strength and light weight is also desirable in other fields such as rock climbing equipment and bicycle components. One interesting use for AA7075-T651 is in the manufacture of M16 rifles for the American military.

## 2.2 Design of Compression Specimen

Figure 2-1 shows geometries of the specimens used in the static and impact compression tests. The shape and dimensions of the compression specimens used are listed in Table 2-2. The reason why the specimen dimensions differ between Al alloys is that the specimens were taken along the thickness direction of rolled plates with different thickness. Following the ASTM Designation E9-89a [5], the slenderness ratio  $h_s/d_s$  (= thickness/diameter) of the static specimen was taken as large as 1.65 by stacking two thin identical specimens to minimize frictional effects at the specimen-anvil interfaces during compression loading. In order to achieve dynamic stress equilibrium in impact specimen during SHPB test, a thin specimen is preferable. Experimental results show that dynamic stress equilibrium cannot be achieved in a very thin specimen. Therefore, the slenderness ratio  $l/d$  of the impact specimen was taken as 0.5~0.8, falling in an appropriate slenderness ratio range between

0.5 and 1.0 suggested by Gray [6] in the conventional SHPB tests. Before testing, the specimen end surfaces were carefully polished with a waterproof #3000 emery paper and buffed with a buffing wheel to ensure smooth surfaces.

### **2.3 Low Strain-Rate Compression Testing**

Static compression tests were conducted using an Instron testing machine (Model 5500R, Norwood, MA, USA) at a crosshead speed of 1mm/min with a 100 kN capacity load cell (see, Fig. 2-2). A picture of Instron testing machine with its schematic diagram is given in Fig. 2-3. For each specimen, at least three repeatable tests were conducted as to confirm the reproducibility of the results. The stacked specimens were loaded up to a given strain and unloaded at the same crosshead speed. Compressive strains were determined from specimen displacements measured with a 50 mm strain gage extensometer (Instron 2620-601, MA, USA). Special care was taken to minimize the frictional effects between the specimen ends and cylindrical anvils (Instron, #2501-082) of 50mm diameter using MoS<sub>2</sub> lubricant.

### **2.4 High Strain-Rate Compression Testing**

Gray [6] provides a comprehensive overview of the SHPB techniques which include: the history, implementation, calibration and data reduction methods. A picture of the SHPB apparatus [8] (measurement system not shown) and its schematic illustration are given in Fig. 2-4. The apparatus consists of two bearing steel (JIS SUJ 2) input and output bars of 1500 mm in length, 12 mm or 16

mm in diameter. Figure 2-5 shows the compression specimen is sandwiched between the input and output bars. The mechanical properties of a striker bar and the input/output bars are listed in **Table 2-2** while the dimensions of the striker bar and input/output bars are given in **Table 2-3**. Figure 2-6 depicts a Lagrangian  $x-t$  diagram illustrating the details of the elastic wave propagation in the input and output bars. The specimen was held in place between the input and output bars by applying a very small pre-compression load with turning of the head of a support block. As in the static tests, lubricant (or petroleum jelly) was applied to the bar/specimen interfaces to reduce the frictional effects. A pulse shaping technique [8] was applied to generate well-defined incident strain pulses without higher frequency components in the input bar. Namely, a 0.2 mm thick 1050 Al disk of nearly 10 mm in diameter was attached onto the impact (left) end of the input bar using a thin layer of petroleum jelly.

When the input bar is impacted with the striker bar launched through a gun barrel, a compressive strain pulse ( $\epsilon_i$ ) is generated in the input bar and travels towards the specimen. At the bar/specimen interface, because of the impedance mismatch, part of the strain pulse is reflected back into the input bar ( $\epsilon_r$ ) and the remaining part is transmitted through the specimen into the output bar ( $\epsilon_t$ ). The incident, reflect and transmitted strain pulses are then recorded with two pairs of semiconductor strain gages (Kyowa: KSP-2-120-E3) mounted on the input and output bars. The output signals from the strain gages are fed through a bridge circuit into a 10-bit digital storage oscilloscope (Iwatsu: DS-9121), where the signals are digitized and stored at a sampling time of 1  $\mu$ s/word. The positions are shown schematically as Gage No. 1 and Gage No. 2, respectively in Figure 2- 4 (b). The digitized data are then transferred to a 32-bit personal computer for data processing.

When elastic strain pulses travel along the SHPB bars, the pulses are approximately one-dimensional. Across the one-dimensional stress-wave front, the conservation of mass, momentum, and energy should be satisfied. The conservation of mass yields the relationship between the particle velocity ( $v$ ) and the strain ( $\epsilon$ ) as

$$v(t) = c_0 \epsilon(t) \quad (1)$$

where  $c_0 (= \sqrt{E_0 / \rho_0})$  is the elastic wave speed in the bar,  $E_0$  and  $\rho_0$  are Young's modulus and the mass density of the bar. Equation (1) can be applied to express the particle velocities at both interfaces between the bars and the specimen as

$$v_1(t) = c_0 \{\epsilon_i(t) - \epsilon_r(t)\} \quad (2)$$

$$v_2(t) = c_0 \epsilon_t(t) \quad (3)$$

where  $\epsilon_i$ ,  $\epsilon_r$  and  $\epsilon_t$  correspond to the incident, reflected, transmitted strain pulses, respectively, and subscripts 1 and 2 denotes the left and right interfaces. The strain rate in the specimen with the thickness of  $h_s$  is given by

$$\dot{\epsilon}(t) = \frac{v_1(t) - v_2(t)}{h_s} = \frac{c_0}{h_s} \{\epsilon_i(t) - \epsilon_r(t) - \epsilon_t(t)\} \quad (4)$$

Integration Eq. (4) with respect to time  $t$  yields the strain in the specimen

$$\varepsilon(t) = \int_0^t \varepsilon(\tau) d\tau = \frac{c_0}{h_s} \int_0^t \{\varepsilon_i(\tau) - \varepsilon_r(\tau) - \varepsilon_i(\tau)\} d\tau \quad (5)$$

The axial forces on both interfaces of the specimen are calculated as

$$P_1(t) = E_0 A_0 \{\varepsilon_i(t) + \varepsilon_r(t)\} \quad (6)$$

$$P_2(t) = E_0 A_0 \varepsilon_i(t) \quad (7)$$

where  $A_0$  is the cross-sectional area of the bars. The stress in the specimen is given by

$$\sigma(t) = \frac{A_0}{2A_s} E_0 \{(\varepsilon_i(t) + \varepsilon_r(t) + \varepsilon_i(t))\} \quad (8)$$

where  $A_s$  is the initial cross-sectional area of the specimen. Under the assumption of dynamic stress equilibrium within the specimen, this means that the force at the input bar-specimen interface ( $P_1$ ) must be equal to the force at the output bar- specimen interface ( $P_2$ ), we obtain

$$\sigma_1(t) = \sigma_2(t) \text{ or } \varepsilon_i(t) + \varepsilon_r(t) = \varepsilon_t(t) \quad (9)$$

Therefore, Eqs. (4), (5), and (8) can be simplified as

$$\dot{\varepsilon}(t) = -2 \frac{c_0}{h_s} \varepsilon_r(t) = \left( -2 \frac{v_R(t)}{h_s} \right) \quad (10)$$

$$\varepsilon(t) = -2 \frac{c_0}{h_s} \int_0^t \varepsilon_r(t) dt \quad (11)$$

$$\sigma(t) = \frac{A_0}{A_s} E_0 \varepsilon(t) \quad (12)$$

All the nominal strain, strain rate and stress are converted to the respective true values under the assumption of constant specimen volume as

$$\varepsilon_a(t) = -\ln\{1 - \varepsilon(t)\} \quad (13)$$

$$\dot{\varepsilon}_a(t) = \frac{\dot{\varepsilon}(t)}{1 - \varepsilon(t)} \quad (14)$$

$$\sigma_a(t) = \sigma(t) \{1 - \varepsilon(t)\} \quad (15)$$

Eliminating time  $t$  through Eq. (13) to Eq. (15) yields the true compressive stress-strain and strain rate-strain relations. The compressive stress and strain are assumed to be positive in this study. Note that the conservation of energy is not involved in the calculation of stress-strain data.

## 3 Results and Discussion

### 3.1 SHPB Test Results

A number of the SHPB tests were performed on the three different aluminum alloys (AA2024-T3, AA6061-T6 and AA7075-T651) for aircraft structures at room temperature. Figure 3- 1 indicates typical oscilloscope records from the SHPB test on the AA2024-T3 at a striker - bar impact velocity of  $V_s = 11.1$  m/s. The top trace gives the incident and reflected strain pulses ( $\epsilon_i$  and  $\epsilon_r$ ), and the bottom trace gives the transmitted strain pulse ( $\epsilon_t$ ). The recorded signal data are neither smoothed nor averaged electronically. The dynamic stress-strain curve is determined from the Hopkinson bar data analysis. It is found from Fig. 3- 2 that the assumption of dynamic stress equilibrium within the specimen is validated.

Figure 3- 3 shows the static and dynamic true compressive stress-strain behavior of AA2024-T3. It is seen that AA2024-T3 exhibits almost no strain rate dependence up to a strain rate of about 1000/s, which is quite consistent with test data of Hodowany *et al.* [9]. The strain rate does not remain constant and, hence, the average strain rate during loading process is given as the area under the dynamic strain rate-strain curve divided by the maximum strain. Figure 3- 4 presents the static and dynamic true compressive stress-plastic strain curves redrawn using  $\epsilon_p = \epsilon - \sigma / E$  for AA2024-T3. From this figure, we can easily determine the yield stress  $\sigma_Y$  and strain hardening rate  $H'$  at low and high rates of strain. There is a little difference between respective  $\sigma_Y$  and  $H'$  values at low and high rates of strain. According to energy analysis given in **APPENDIX**, the maximum plastic strain and strain rates in the SHPB specimen can be predicted from Eqs. (A14), (A15) or (A19), (A20),

depending on material models used (see Figs. A- 1 and A- 2). The yield stress  $\sigma_y$  and strain hardening rate  $H'$  at the low strain rate determined from Fig. 3- 4 are used in the energy analysis. The other material parameters needed for the energy analysis are summarized in **Tables 2- 1 to 2- 3**. Figure 3- 5 indicates the static and dynamic true compressive stress-strain characteristics of AA6061- T6. Unlike AA2024- T3, the flow stress of AA6061- T3 increases slightly with increasing strain rate and typical strain hardening behavior is seen. Similarly, Fig. 3- 6 shows the static and dynamic true compressive stress-plastic strain curves of AA6061- T6 redrawn from Fig. 3- 5. Figure 3- 7 shows the static and the dynamic true compressive stress-strain behavior of AA7075-T651. It is found that AA7075- T651 exhibits very slightly rate dependence in the initial plastic portion of the dynamic compressive stress-strain curve and typical strain hardening behavior. Figure 3- 8 displays the static and dynamic true compressive stress-plastic strain curves of the AA7075-T651 redrawn from Fig. 3- 7.

It is shown that the maximum plastic strain and strain rate in the SHPB specimens can approximately be predicted from energy analysis based on rate-independent plasticity. The experimental and predicted maximum plastic strains and strain rates for three different aluminum alloys are summarized in **Table 3- 1**. The present energy analysis neglects the kinetic energy,  $K_e$ , of the specimen, thus yielding an overestimation of the average strain rate,  $\dot{\epsilon}$  and maximum plastic strain,  $\epsilon_{P(max)}$ , in the SHPB specimens. From the experimental and predicted results of the strain rates for three different aluminum alloys, the predicted strain rates of the AA2024-T3 and AA7075-T651 gives better agreement with the experimental results compared to AA6061- T6. This shows that both AA2024-T3 and AA7075-T651 show almost no strain rate dependence and, hence, can be regarded

as rate independent materials. In the other hand, AA6061-T6 can be regarded as rate dependent materials. These differences are due to the microstructure of each aluminum alloys where precipitation strengthening happened as it is found that three high-strength aluminum alloys (AA2024-T3, AA6061-T6, and AA7075-T651) exhibits typical strain hardening behavior of the material. The microstructure of each aluminum alloys are elaborated in details in the next section.

### **3.2 Observation of Macrostructure and Microstructure in Test Materials**

Perfectly (or ideally) plastic behavior of material subjected to uniaxial loading yields at a constant stress. During plastic flow under general multiaxial loading, the stress state can move along the yield surface, but the surface itself remains unchanged [10]. However, in reality the microstructure (see Figs. 3- 10) of the material changes as plastic flow continues, and this results in a change of the properties observable at the macro scale (see Figs. 3- 9). Under uniaxial loading, the stress transmitted by a yielding material can increase or decrease. An increase of the yield stress is referred to as hardening, and its decrease is called softening. Typically, many materials initially harden and later soften. For convenience, however, we will sometimes use the term 'hardening' in a broader sense, meaning yield stress changes of any sign, negative hardening being equivalent to softening. During hardening, the elastic domain undergoes a certain evolution. The elastic domain of a virgin material is bounded by the initial yield surface, also called the elastic limit envelope. Due to microstructural changes in the material induced by plastic flow, the elastic domain changes its size or position, or both. Its boundary at an intermediate state is usually called a loading surface. The microstructural changes in the material induced by plastic flow are due to precipitation hardening [11], on the other hand, involves the strengthening of alloys by coherent precipitates which are capable of being sheared by dislocations.

This is because, the interaction between dislocations and the internal stresses produced by misfitting coherent precipitates.

## 4 Conclusions

In order to predict the maximum plastic strain and strain rate in the SHPB specimens from energy analysis based on strain-rate independent plasticity, the dynamic compressive stress-strain curves for the three different aluminum alloys (AA2024-T3, AA6061-T6, and AA7075-T651) have been determined with the SHPB set-up. The corresponding static stress-strain curves were measured using the Instron testing machine. From the present work, we can draw the following conclusions:

- 1) Both AA2024-T3 and AA7075-T651 show almost no strain-rate dependence and, hence, the present analysis is applicable within experimental accuracy.
- 2) AA6061-T6 cannot be regarded exactly as the rate independent material. The maximum plastic strain and strain rate in the SHPB specimens cannot accurately predicted from energy analysis.
- 3) The three high-strength aluminum alloys exhibit typical strain hardening behavior. Therefore, the rigid plastic-strain hardening material model is more appropriate than the rigid perfectly-plastic material model.
- 4) The present energy analysis neglects the kinetic energy,  $K_e$ , of the specimen, thus yielding an overestimation of the average strain rate,  $\dot{\epsilon}$  and maximum plastic strain,  $\epsilon_{P(max)}$ , in the SHPB specimens.

## Appendix

### A.1 Energy analysis in the SHPB

When the strain pulse travels in an elastic bar, it produces both elastic deformation and motion (particle velocity) in the bar. The energy for the elastic deformation is defined as elastic strain energy. The energy associated with the particle velocity is the kinetic energy. The energy carried by the strain pulse generally consists of both the elastic strain energy and the kinetic energy. The elastic strain energy  $U_I$  of the incident strain pulse can be expressed as

$$U_I(t) = \frac{1}{2} (A_0 c_0 \Delta t) E_0 \varepsilon_i^2(t) \quad (\text{A1})$$

The mass  $m$  and the particle velocity  $v_I$  of the deformed portion in the input bar are given by, respectively

$$m = \rho_0 A_0 c_0 \Delta t \quad (\text{A2})$$

$$v_I(t) = c_0 \varepsilon_i(t) \quad (\text{A3})$$

where  $\Delta t$  is a duration time of the incident strain pulse given by  $\Delta t = 2l_{ST}/c_0$ . It is very important to understand the propagation of elastic waves [9] in cylindrical bars. This is required for the analysis of Hopkinson bar experiments. When one impacts a cylindrical bar (input bar) with a cylindrical projectile (striker bar) of length  $l_{ST}$ , one would expect a rectangular pulse of length  $2l_{ST}$

propagating through the bar if the bar and striker bar are of the same material. This is shown schematically in Fig. A- 1. The impact produces compressive waves propagating at velocities  $c_0$  into striker bar and target. As the compressive wave reaches the end of the projectile, it reflects back and this determines the length of the pulse,  $\Lambda = 2l_{ST}$ . The velocity of the interface, equal to the particle velocity, can be calculated from the conservation of momentum equation (momentum prior to impact,  $\rho_0 A_0 l_{ST} v_s(t)$  equals to momentum after impact,  $\rho_0 A_0 \Lambda v_I(t) = 2\rho_0 A_0 l_{ST} v_I(t)$ ). Thus, the particle velocity of the deformed portion in the input bar can also be written from the striker bar velocity  $v_s$  as

$$v_I(t) = \frac{v_s(t)}{2} \quad (A4)$$

Therefore, the strain energy  $U_I(t)$  can be rewritten using Eqs. (A2) and (A3) as

$$U_I(t) = \frac{1}{2} m v_I^2(t) \quad (A5)$$

The kinetic energy  $K_I(t)$  of the incident strain pulse can be expressed as

$$K_I(t) = \frac{1}{2} m v_I^2(t) \quad (A6)$$

The total energy  $W_I(t)$  carried by the incident strain pulse can be calculated

$$W_I(t) = U_I(t) + K_I(t) = mv_I^2(t) \quad (\text{A7})$$

When the input and output bars are made of the same material and diameter, the total energies,  $W_R$  and  $W_T$  associated with the reflected and transmitted strain pulses, respectively, can be similarly written as

$$W_R(t) = mv_R^2(t) \quad (\text{A8})$$

$$W_T(t) = mv_T^2(t) \quad (\text{A9})$$

The absorbed energy in the specimen can easily be calculated by neglecting the kinetic energy  $K_e(t)$  as

$$U_e(t) = W_I(t) - W_R(t) - W_T(t) \quad (\text{A10})$$

We consider two simplified rate-independent material models in the energy analysis.

## A.2 Strain rate independent models

### A.2.1 Rigid perfectly-plastic material model[12]

For a rigid perfectly-plastic material model shown in Fig. A- 2, the energy stored in the SHPB specimen or absorbed energy can be written as

$$U_e(t) = A_S h_S \sigma_Y \varepsilon_P(t) \quad (\text{A11})$$

By substituting Eqs. (A7)- (A9), (A11) into Eq. (A10) and using the relation of  $v_I + v_R = v_T$ , the particle velocity of reflected and transmitted strain pulses can be written as

$$v_R(t) = -\left( v_I(t) - \frac{A_S}{A_0} \frac{\sigma_Y}{\rho_0 c_0} \right) \quad (\text{A12})$$

$$v_T(t) = \frac{A_S}{A_0} \frac{\sigma_Y}{\rho_0 c_0} \quad (\text{A13})$$

Substituting Eq. (A12) into Eq. (10) leads to the strain rate  $\dot{\varepsilon}$  and then the total plastic strain  $\varepsilon_p$  in the specimen as

$$\dot{\varepsilon}(t) = \frac{-2}{h_s} v_R(t) = \frac{2}{h_s} \left( v_I(t) - \frac{A_S}{A_0} \frac{\sigma_Y}{\rho_0 c_0} \right) \quad (\text{A14})$$

$$\varepsilon_p(t) = \dot{\varepsilon} \Delta t = -\frac{2v_R(t)}{h_s} \Delta t = \frac{2}{h_s} \left( v_I(t) - \frac{A_S}{A_0} \frac{\sigma_Y}{\rho_0 c_0} \right) \Delta t \quad (\text{A15})$$

### A.2.2 Rigid plastic-strain hardening material model[12]

For a rigid plastic-strain hardening material model with the yield stress  $\sigma_Y$  and the strain hardening rate  $H'$  depicted in Fig. A- 3, the energy stored in the SHPB specimen or absorbed energy can be written as

$$U_e(t) = A_S h_S \left\{ \sigma_Y \varepsilon_p(t) + \frac{H'}{2} \varepsilon_p^2(t) \right\} \quad (\text{A16})$$

By substituting Eqs. (A7)- (A9), (A16) into Eq. (A10) and using  $v_I + v_R = v_T$ , the particle velocity of reflected and transmitted strain pulses can be expressed as

$$v_R(t) = -\frac{v_I(t) - \frac{A_S \sigma_Y}{A_0 \rho_0 c_0}}{1 + \frac{A_S H' \Delta t}{\rho_0 A_0 C_0 h_S}} \quad (\text{A17})$$

$$v_T(t) = v_I(t) - \frac{v_I(t) - \frac{A_S \sigma_Y}{A_0 \rho_0 c_0}}{1 + \frac{A_S H' \Delta t}{\rho_0 A_0 C_0 h_S}} \quad (\text{A18})$$

Similarly, substituting Eq. (A17) into Eq. (10) yields the strain rate  $\dot{\varepsilon}$  and then the total plastic strain  $\varepsilon_p$  in the specimen as

$$\dot{\varepsilon}(t) = \frac{-2}{h_S} v_R(t) = \frac{2}{h_S} \left\{ \frac{v_I(t) - \frac{A_S \sigma_Y}{A_0 \rho_0 c_0}}{1 + \frac{A_S H' \Delta t}{\rho_0 A_0 c_0 h_S}} \right\} \quad (\text{A19})$$

$$\varepsilon_p(t) = \dot{\varepsilon}(t) \Delta t = -\frac{2v_R(t)}{h_S} \Delta t = \frac{2}{h_S} \left\{ \frac{v_I(t) - \frac{A_S \sigma_Y}{A_0 \rho_0 c_0}}{1 + \frac{A_S H' \Delta t}{\rho_0 A_0 c_0 h_S}} \right\} \Delta t \quad (\text{A20})$$

## References

- [1] Kolsky, H.: An Investigation of the Mechanical Properties of Materials at Very High Rates of Loading, *Proc. Phys. Soc.*, **B62**, (1949), 676-700.
- [2] Chen, W. and Song, B.: *Split Hopkinson (Kolsky) Bar*, Springer, New York (2011).
- [3] Yokoyama, T.: Characterization of Impact Stress-Strain Behavior of Laminated Composites-A Review- Focused on the Split Hopkinson Pressure Bar Techniques (in Japanese), *Journal of the JSEM*, **6-2** (2006), 105-114.
- [4] Song, B. and Chen, W.: Energy for Specimen Deformation in a Split Hopkinson Pressure Bar Experiment, *Exp. Mech.*, **46** (2006), 407-410.
- [5] ASTM E9-89a: *Annual Book of ASTM Standards*, Section 3, Vol. 03.01, p. 101, American Society for Testing and Materials, Philadelphia (1995).
- [6] Gray, G.T. III: Classic Split-Hopkinson Pressure Bar Testing, *ASM Handbook, Vol.8, Mechanical Testing and Evaluation*, 462-476, ASM International, Materials Park, Ohio (2000).
- [7] Frew, D. J., Forrestal, M.J., and Chen, W.: Pulse Shaping Techniques for Testing Brittle Materials with a Split Hopkinson Pressure Bar, *Exp. Mech.*, **42-1**, (2002), 93-106.
- [8] Nakai, K., and Yokoyama, T.: "Strain Rate Dependence of Compressive Stress-Strain Loops of Several Polymers," *JSME Journal of Solid Mechanics and Materials Engineering*, **2-4**, (2008), 557-566.
- [9] Meyers, M.A.: *Dynamic Behavior of Materials*, John Wiley & Sons, New York (1994), 54-55.
- [10] Hodowany, J., Ravichandran, G., Rosakis, A.J. and Rosakis, P.: Partition of Plastic Work into

Heat and Stored Energy in Metals, *Exp. Mech.*, **40** (2000), 113-123.

[11] Dieter, G. E., Jr.: *Mechanical Metallurgy*, McGraw-Hill, London (1988), 212.

[12] Marciniak, Z., Duncan, J. L. and Hu, S. J.: *Mechanics of Sheet Metal Forming*, Edward Arnold, London (1992), 37.